Channel waveguide lasers in bulk Tm:LiYF 4 produced by deep diamond-saw dicing

Pavel Loiko, Ludovic Gauthier-Manuel, Gurvan Brasse, Esrom Kifle, Lauren Guillemot, A. Braud, Abdelmjid Benayad, Vivien Menard, Patrice Camy

Channel waveguide lasers in bulk Tm:$LiYF_4$ produced by deep diamond-saw dicing

PAVEL LOIKO,[1] LUDOVIC GAUTHIER-MANUEL,[2] GURVAN BRASSE,[1] ESROM KIFLE,[1] LAUREN GUILLEMOT,[1] ALAIN BRAUD,[1] ABDELMJID BENAYAD,[1] VIVIEN MENARD,[1] AND PATRICE CAMY[1,*]

[1]*Centre de recherche sur les Ions, les Matériaux et la Photonique (CIMAP), UMR 6252 CEA-CNRS-ENSICAEN, Université de Caen, 6 Boulevard du Maréchal Juin, 14050 Caen, France*
[2]*FEMTO-ST Institute, 15B avenue des Montboucons, 25030 Besançon Cedex, France*
**patrice.camy@ensicaen.fr*

Abstract: We report on a novel approach to fabricate channel (ridge) waveguides (WGs) in bulk crystals using precision diamond saw dicing. The channels feature a high depth-to-width aspect ratio (deep dicing). The proof-of-the-concept is shown for a Tm^{3+}:$LiYF_4$ fluoride crystal. Channels with a depth of 200 μm and widths of 10–50 μm are diced and characterized by confocal laser microscopy revealing a r.m.s. roughness of the walls well below 100 nm. The channels obtained possess waveguiding properties at ~815 nm with almost no leakage of the guided mode having a vertical stripe intensity profile into the bulk crystal volume and relatively low propagation losses (0.20-0.43 dB/cm). Laser operation is achieved in quasi-CW regime by pumping at 780 nm. The maximum peak output power reaches 0.68 W at ~1.91 μm with a slope efficiency of 53.3% (in σ-polarization). The proposed concept is applicable to a variety of laser crystals with different rare-earth dopants.

1. Introduction

Fluoride crystals doped with rare-earth ions (RE^{3+}) are attractive for development of efficient power-scalable waveguide (WG) lasers emitting in the Short Wavelength Infrared (SWIR) spectral range, an, in particular, at ~2 μm and beyond) [1-5]. As host matrices, they provide good thermal properties (e.g., the thermal conductivity of undoped $LiYF_4$, $\langle\kappa\rangle$ = 6.0 $Wm^{-1}K^{-1}$) [6], broadband transparency (0.15-7.5 μm for $LiYF_4$), low refractive index (n_o = 1.443 and n_e = 1.465 for $LiYF_4$ at ~1.9 μm) [7] and low phonon energies ($h\nu_{ph}$ = 446 cm^{-1} for $LiYF_4$) [8]. The latter determines weak non-radiative relaxation and long upper laser level lifetimes of the RE^{3+} ions [9]. An example of efficient fluoride laser material is RE^{3+}-doped lithium yttrium fluoride crystal, $LiYF_4$ [10-12]. This material belongs to the tetragonal crystal class (sp. gr. $I4_1/a$) and it exhibits natural birefringence [7]. It also offers a single rare-earth site (the Y^{3+} one) and can be doped with the RE^{3+} ions in high concentrations [13]. The technology of growth of bulk RE^{3+}-doped $LiYF_4$ crystals by the Czochralski (Cz) method is well-developed [14].

Nowadays, a common way to produce crystalline RE^{3+}-doped $LiYF_4$ WGs is the Liquid Phase Epitaxy (LPE) [15]. In this way, high optical quality thin crystalline films of RE^{3+}:$LiYF_4$ are achieved on undoped oriented bulk $LiYF_4$ substrates resulting in a planar WG geometry [16]. Consequently, a microstructuring step is required to fabricate channel WGs with a well-defined transverse profile of the refractive index leading to the single-transverse-mode operation. One known method of microstructuring of LPE-grown crystalline films is the ion beam milling leading to relatively low propagation losses (δ_{loss} ~0.11 dB/cm) [17]. However, it is rather complicated from the technological point of view. Recently, we demonstrated the suitability of precision diamond saw dicing for microstructuring of LPE-grown Tm^{3+}-doped $LiYF_4$ crystalline thin-films [18]. A Tm^{3+}:$LiYF_4$ channel WG laser generated 1.30 W at 1880 nm with a slope efficiency of 80% with respect to the absorbed pump power and a low laser threshold of 80 mW.

In the present work, we aimed to extend this technology to direct fabrication of optical WGs in *bulk* crystals. A special geometry of WGs with a high depth-to-width aspect ratio (referred as deep dicing) was selected. In this way, the mode confinement is expected to be provided by the refractive index contrast at the crystal / air interfaces and an additional refractive index variation due to the photo-elastic effects originating from stresses induced by mechanical dicing.

So far, precision diamond saw dicing was used for fabrication of optical WGs in various optical materials, Table 1. Chen *et al.* applied this method for fabrication of ridges in polymer films deposited on SiO_2/Si wafers and doped with fluoride nanoparticles (Er^{3+},Yb^{3+}:$NaYF_4$); optical gain at ~1.5 μm was reported [19]. Waeselmann *et al.* patterned Nd^{3+}:α-Al_2O_3 (sapphire) thin films produced by pulsed laser deposition (PLD). Laser operation was achieved: the WG laser generated 322 mW at 1092 nm with a slope efficiency of ~12% probably due to the high losses of ~6 dB/cm [20]. Earlier, Jia *et al.* fabricated ridge WGs in bulk Nd^{3+}:$Y_3Al_5O_{12}$ single-crystals subjected to swift heavy ion irradiation and extracted 84 mW of output power at 1064 nm with a slope efficiency of 43% corresponding to lower δ_{loss} = 1.7 dB/cm [21]. Kifle *et al.* structured LPE-grown anisotropic Tm:$KY_{1-x-y}Gd_xLu_y(WO_4)_2$ thin films and generated 262 mW at 1833 nm with a high slope efficiency of 82.6% and moderate δ_{loss} = 1.1 dB/cm [22]. Finally, WGs in irradiated $LiNbO_3$ and $KTiOPO_4$ crystals were also fabricated by diamond saw dicing [24,25], featuring WG propagation losses of ~1 dB/cm. These structures were used for second-harmonic generation leading to green emission.

Table 1. Optical Waveguides Produced by Diamond Saw Dicing

Material	Form	Size, μm	Aspect ratio (y/x)	δ_{loss}, dB/cm	Ref.
Polymer + Er,Yb:$NaYF_4$	Spin-coated film	10(x)×3(y)	0.30	2.9	[19]
Nd:α-Al_2O_3	PLD film	41(x)×2.6(y)	0.06	~6	[20]
Nd:$Y_3Al_5O_{12}$	Irradiated crystal	22(x)×9(y)	0.41	1.7	[21]
Tm:$KY_{1-x-y}Gd_xLu_y(WO_4)_2$	LPE film	61(x)×15.3(y)	0.25	1.1	[22]
Tm:$LiYF_4$	LPE film	30(x)×30(y)	1.0	**0.28**	[18]
$KTiOPO_4$	Irradiated crystal	25(x)×30(y)	1.2	1.04	[23]
MgO:$LiNbO_3$	Irradiated crystal	8.5(x)×30(y)	3.5	2.14	[24]
$LiNbO_3$	Ion-indiffused crystal	6(x)×>20(y)	**>3.3**	0.5	[25]
Tm:$LiYF_4$	Bulk crystal	10-50(x)×200(y)	**4-20**	**0.1-0.4**	*

*This work.

Note that all the previous studies [19-24] focused on near-surface dicing (with the depth not exceeding few tens of μm) corresponding to small aspect ratios (depth / width, or y/x) of about unity or much less. High aspect ratio (e.g., top width: 1 μm, depth: 500 μm) WGs were reported only in lithium niobate [25], however, reasonably low propagation losses of 0.5 dB/cm were observed for less exaggerated structures, cf. Table 1.

2. Fabrication of waveguides

2.1 Diamond saw dicing

As a reference material for proof-of-the-concept, we selected the tetragonal Tm^{3+}:$LiYF_4$ crystal. It was grown by the conventional Czochralski (Cz) method and doped with 4.0 at.% Tm (the actual ion concentration: N_{Tm} = 5.50×10^{20} cm^{-3}). A rectangular sample was cut for light propagation along the crystallographic ***a***-axis (***a***-cut) with a thickness (t) of 7.0 mm and an aperture of 3.5(***c***)×10 mm^2. The input and output faces and the top surface of the sample were polished to laser quality and remained uncoated.

Then, the top surface was subjected to precision diamond saw dicing resulting in fabrication of surface channels (ridges) with a depth of 200 μm along the ***c***-axis and a varied width of 10–

50 μm (with a step of 10 μm), Fig. 1. Such widths are similar to those achieved in LPE films or single crystals by other micro-structuring methods, such as ion beam milling or fs direct laser writing. The step of 10 μm was selected from the point of view of convenience in discriminating the guides from each other, there were no technical limitation for this. The channels propagated through the whole length of the sample. For this purpose, very low grit size blades were selected and calibration processes occurred to ensure the dimensions of the ridges. The channels were separated by about 500 μm, which is sizable but comes from the use of a large blade: it enforces a better stability and minimize vibrations during deep dicing. The end-facets of the crystal sample were not repolished after the dicing, but the dicing process may additionally improve the end-facet quality by cutting the material orthogonally to the ridge thus reducing roughness and ensuring a good verticality of the input/output surfaces.

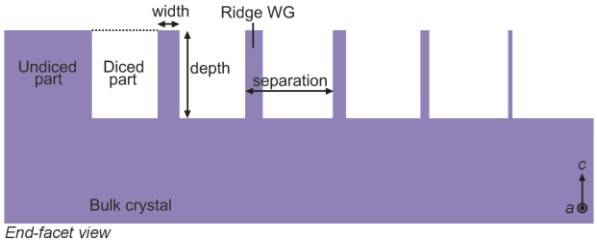

Fig. 1. Scheme of the deep diced ridge WGs in bulk Tm^{3+}:$LiYF_4$ crystal (the end-facet view).

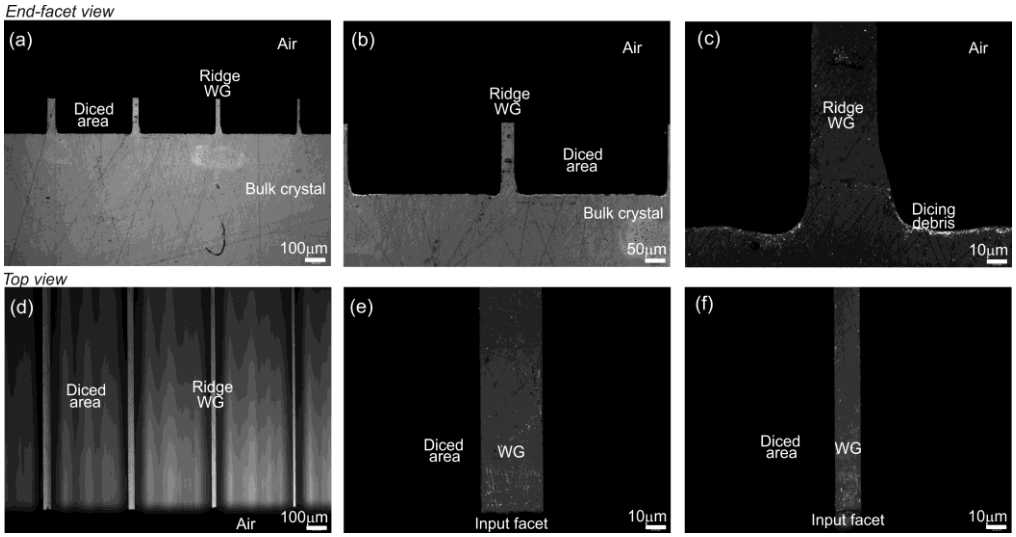

Fig. 2. Confocal laser microscope images of the Tm^{3+}:$LiYF_4$ crystal subjected to precision diamond-saw dicing: (a-c) the end-facet view showing (a) (from left to right) 40 μm, 30 μm, 20 μm and 10 μm wide WGs, (b) a close view in the 30 μm WG and (c) the bottom part of the 30 μm WG; (d-f) the top surface view on (d) (from left to right) 40 μm, 30μm, 20 μm and 10 μm WGs, (e,f) the input facet of (e) 30 μm and (f) 10 μm WG. Reflection mode, λ = 405 nm.

The quality and geometry of channels were inspected with a confocal laser microscope (Sensofar S-neox) equipped with a blue light-emitting diode (LED, λ = 405 nm), Fig. 2. First, we studied one of the end-facets of the sample, showing vertical “pillows” separated by diced regions, Fig. 2(a). No cracks propagating into the guides nor into the bulk crystal volume are observed (the dark lines are due to the polishing of the end-facet of the sample before dicing and they are enhanced because of the observation geometry in reflected light which is sensitive to the surface quality). A close view on one of the fabricated guides (with an intermediate width of 30 μm), Fig. 2(b), reveals vertical walls within about 3/4 of its height. The flatness of the input facet of the guide is similar to that of the bulk crystal, so that no repolishing is required.

In the bottom part of the same guide (at about 1/4 of its height), Fig. 2(c), a rounding is observed and it is asymmetric from left and right diced areas. In this part, small bright spots with a size <0.1 μm are visible and they are interpreted as writing debris. Such rounding in the bottom part of the channels is characteristic for diamond saw dicing and it was also observed in guides diced at small depths [18,22].

Furthermore, the top surface of the sample was observed, Fig. 2(d). The fabricated guides are straight and there are no cracks preventing the light propagation through the whole length of the sample. A lose view on the top surface of two guides (with a width of 30 μm and 10 μm) is shown in Fig. 2(e,f). The ridges have smooth side walls. The r.m.s. surface roughness of the channel walls is well below 100 nm (this value is an upper estimation, limited by the precision of the used method). According to the studies of ridges in lithium niobate, even lower roughness down to ~5 nm is expected.

2.2 Waveguiding properties

The passive waveguiding properties of the fabricated channels were studied at the wavelength of ~815 nm. It is close to the pump wavelength for Tm^{3+}:$LiYF_4$ (780 nm, the $^3H_6 \rightarrow {}^3H_4$ Tm^{3+} transition). The power of the pump beam was maintained to be low (~20 mW) to operate in the small-signal regime avoiding bleaching of the Tm^{3+} absorption. As a laser source, we used a Ti:sapphire laser (3900S, Spectra Physics). Its output (beam quality parameter: $M^2 \approx 1$) was focused into the WGs using an uncoated CaF_2 lens (focal length: f = 40 mm) resulting in a measured spot size $2w_P$ of 30±5 μm (at the $1/e^2$ level). The mode profile at the output facet of the waveguide was reimaged to a CCD camera (BladeCam-XHR, DataRay Inc.) using a short focal length CaF_2 lens (f = 15 mm). The scale calibration for the camera was performed by illuminating the WGs with a known size using a near-IR light source (LED) placed before the focusing lens. The obtained calibration images well matched those obtained with the confocal microscopy yielding an estimated scaling error of less than 3 μm. The polarization of the laser beam in the crystal corresponded to π (***E*** || ***c***, vertical). This polarization was selected because it corresponds to higher absorption and stimulated-emission cross-sections for Tm^{3+} ions in $LiYF_4$.

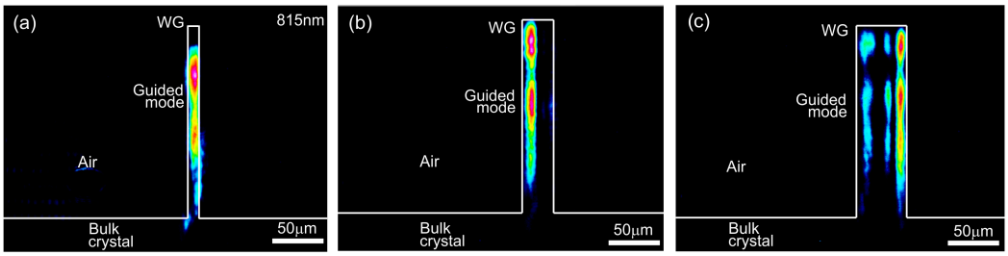

Fig. 3. 2D intensity profiles of the guided pump mode at the output WG facet: the WG width is (a) 10 μm, (b) 30 μm and (c) 50 μm. *While lines* showing the crystal surface are drawn as guides for eyes. λ_P = 815 nm. Pumping in the central part of the input facet. The laser polarization (π) is vertical.

In the first set of experiments, the pump was focused in the central part (with respect to the height) of each guide. The guided modes had a vertical stripe intensity profile well confined within the cross-section of the channel (representing a kind of a rotated planar WG geometry immersed in the air), Fig. 3. The pump modes were spatially multimode for all the guides. For example, for the 10 μm and 20 μm wide WGs, the pump modes were assigned as $TM_{1,0}$ and $TM_{2,0}$, respectively. The appearance of high-order modes was justified by the M^2 measurement along the vertical direction. For wider WGs (30 – 50 μm), the beam was spatially multimode also along the horizontal direction and an asymmetry in the mode was detected: the maximum of light intensity was localized near one of the side walls, Fig. 3(b,c). This is attributed to the

slight asymmetry of the waveguide cross-section induced by dicing, see Fig. 2(b),(c) for example. No leakage of the guided modes into the bulk crystal volume was detected.

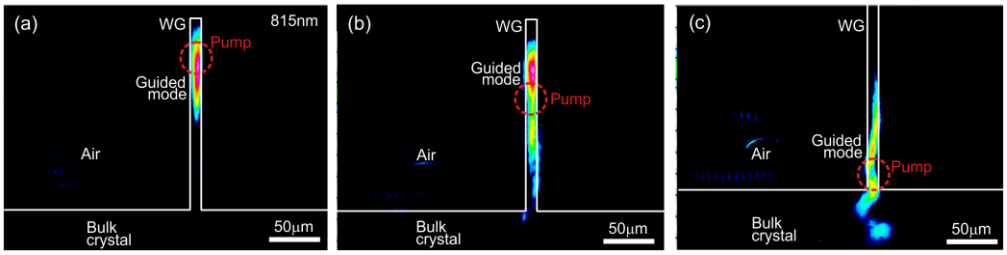

Fig. 4. 2D intensity profiles of the guided pump mode at the output WG facet: focusing of the pump beam in (a) the top part, (b) the medium part and (c) bottom part of the 10 μm wide WG. *While lines* showing the crystal surface are drawn as guides for eyes. *Red dashed circles* indicate the position of the pump beam at the input facet. λ_P = 815 nm. The laser polarization (π) is vertical.

We studied the same WG (with a width of 10 μm) focusing the pump beam in different positions (along the vertical axis) of the input facet, Fig. 4. When focusing the pump near the top of the WG, a vertically extended $TM_{0,0}$ mode was observed, Fig. 4(a). By shifting the position of the pump spot to the center of the guide, the mode extended in the vertical direction corresponding to $TM_{1,0}$, Fig. 4(b). Still, almost no leakage of the pump into the bulk volume was observed. Only when focusing the pump close to the bottom part of the guide, see Fig. 4(c), the modal profile was distorted strongly leaking into the bulk, and a small nearly-circular mode guides under the "pillow" was visible. This distortion is due to the asymmetric rounding of the guide described above.

Let us discuss the guiding mechanism of the fabricated channels. Tetragonal $LiYF_4$ is an optically uniaxial crystal; its optical axis is parallel to the ***c***-axis [7]. There are two principal light polarizations, denoted as π (***E*** ∥ ***c***) and σ (***E*** ⊥ ***c***) and corresponding to the principal refractive indices n_e and n_o. Both polarizations are available for the selected crystal cut (***a***-cut). From the side walls and the top surface, the guiding is provided by the very high refractive index contrast between the crystal (for undoped $LiYF_4$, n_e = 1.4724 at 815 nm) and the air.

The pump geometry ($M^2 \approx 1$, $2w_P$ = 30 μm) corresponded to a Rayleigh length z_R of 1.28 mm in the crystal. Thus, at the output facet of the WG, the pump beam would have a diameter of $(2w_P)_{out}$ ~ 165 μm which agrees with our observations. However, this does not explain the modal profile of the pump along the vertical direction. For the mode confinement of the pump radiation along the vertical direction, we propose two mechanisms: (i) a refractive index variation (increase) in the guide due to the photoelastic effect (a change of the refractive index owing to permanent stresses, in our case, induced by dicing) and (ii) the absorption at the pump wavelength which is stronger for the "wings" of the pump mode which are not able to saturate the Tm^{3+} ions [26]. For Tm^{3+}:$LiYF_4$, the absorption cross-section at 815 nm σ^P_{abs} is 0.41×10^{-21} cm^2 in π-polarization corresponding to a small-signal absorption loss in the studied WGs of 0.7 dB (in a single-pass).

In a similar manner, one may explain the guiding of the laser mode. Note that the $^3F_4 \rightarrow {}^3H_6$ laser transition of Tm^{3+} ions represents a quasi-three-level laser scheme with reabsorption. For example, for lasing in π-polarization, the stimulated-emission (SE) cross-section at the peak emission wavelength of ~1880 nm σ_{SE} is 4.0×10^{-21} cm^2 and the reabsorption cross-section σ^L_{abs} is 0.41×10^{-21} cm^2. Thus, the gain-guiding (the reabsorption in the non-pumped areas of the WG) can be in part responsible for the mode confinement along the vertical direction [27,28]. The second possible reason is the photo-elastic effect. In Fig. 5, we analyzed the 10 μm wide WG using a mode calculator (a variational mode solver based on quasi-analytical vectorial slab mode expansion) [29]. The minimum refractive index variation (increase) in the upper part of the WG with respect to its bottom part and the bulk volume Δn which can support the

fundamental mode ($TM_{0,0}$) at 1880 nm is ~2.5×10^{-3}, Fig. 5(b). The corresponding pump mode at 780 nm ($TM_{1,0}$) is shown in Fig. 5(a) in agreement with the experiment.

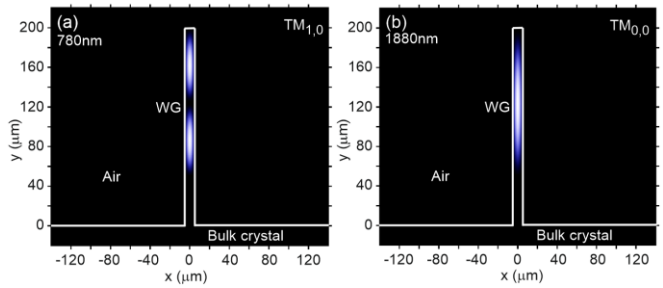

Fig. 5. Simulated 2D intensity mode profiles in the 10 μm wide WG at the light wavelength of (a) 780 nm (pump, $TM_{1,0}$ mode) and (b) 1880 nm (laser, $TM_{0,0}$ mode). The light polarization is vertical. The refractive index increase in the guide Δn is ~2.5×10^{-3}, n_e = 1.4728 (780 nm) and n_e = 1.4652 (1880 nm).

The WG propagation losses δ_{loss} at 815 nm were estimated by observing the top surface of the sample with a CCD camera and detecting the intensity of the scattered pump light along the WG (in the longitudinal direction). An example of this evaluation for the 20 μm and 50 μm wide WGs is shown in Fig. 6. The on-axis intensity of the pump radiation changed according to the equation $I(z) = I_0\times\exp(-\delta_{tot}z)$, where $\delta_{tot} = \alpha_{abs} + \delta_{loss}$ is the total loss coefficient, $\alpha_{abs} = \sigma^{P}_{abs}N_{Tm}$ = 0.23 cm^{-1} is the small-signal absorption coefficient at the pump wavelength and z is the axial coordinate. The origin of strong dispersion of the data points in the end of the guides is non-uniform reflection of scattered light from the silver paint used for mounting the sample. The δ_{loss} monotonously increases for more narrow WGs, from 0.20±0.03 dB/cm for the 50 μm wide WG to 0.43±0.04 dB/cm for the 10 μm wide one, Table 2. This is explained by stronger interaction of the pump mode with the side walls of the WGs containing small defects causing light scattering.

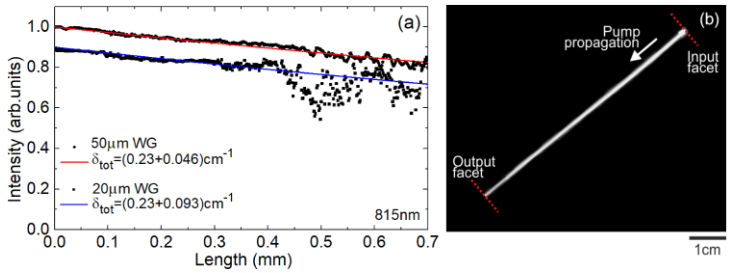

Fig. 6. (a) Longitudinal distribution of the intensity of pump radiation at 815 nm in the 20 μm and 50 μm wide WGs: *symbols* – experimental data, *curves* – their exponential fits using a total loss coefficient $\delta_{tot} = \alpha_{abs} + \delta_{loss}$; (b) The corresponding 2D intensity map from a CCD-camera for the 50 μm wide WG.

Under pumping at 780 nm, the channels provided an intense polarized luminescence at ~1.9 μm due to the $^3F_4 \rightarrow {}^3H_6$ Tm^{3+} transition. The spectral properties were similar to those of the bulk crystal.

3. Laser operation

3.1 Laser set-up

The scheme of the WG laser is shown in Fig. 7. As a pump source, we used a CW Ti:Sapphire laser delivering about 3.2 W of linearly polarized output at 780 nm in a fundamental mode ($M^2 \approx 1$). This wavelength corresponded to the local peak in the absorption spectrum of Tm^{3+}:$LiYF_4$ crystal (the $^3H_6 \rightarrow {}^3H_4$ Tm^{3+} transition). The pump polarization was set to be vertical (π-

polarization in the crystal). The incident pump power was varied by a rotatory λ/2 plate and a Glan-Taylor polarizer. The pump beam was focused by an uncoated CaF_2 lens (f = 40 mm, T = 93.8%) providing a pump spot diameter at the input face of the WG $2w_P$ of 30±5 μm. For quasi-CW pumping, the pump beam was modulated using a mechanical chopper (frequency: 10 Hz, duty cycles ranging from 1:2 to 1:12).

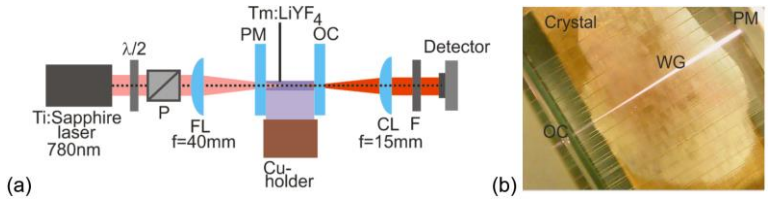

Fig. 7. (a) Scheme of the waveguide laser set-up: λ/2 – half-wave plate, P – Glan-Taylor polarizer, FL and CL – focusing and collimating lenses, respectively, PM – pump mirror, OC – output coupler, F – cut-off filter; (b) top view photograph of the 50 μm wide WG pumped at 780 nm, P_{inc} = 1.0 W, the *bright trace* corresponds to Tm^{3+} upconversion luminescence.

The Tm^{3+}:$LiYF_4$ crystal with the surface guides was mounted on a Cu-holder using a silver paste to improve the thermal contact from the bottom part of the sample. The holder was passively cooled. The crystal was placed in a simple linear plano-plano cavity. It was formed by a flat pump mirror (PM) coated for high transmission (HT, T = 99.4%) at ~0.78 μm and for high reflection (HR, R > 99.9%) at 1.60-2.02 μm, and a set of flat output couplers (OCs) with a transmission at the laser wavelength T_{OC} ranging from 2% to 50%. Both cavity mirrors were gently pressed towards the WG end-facets. No index-matching liquid was used to avoid damaging the optical surfaces. The geometrical cavity length was 7.0 mm. The pump beam was focused into the WGs through the PM.

To filter out the residual (non-absorbed or non-coupled) pump after the OC, a long-pass filter (FEL900, Thorlabs) was used. The laser emission spectra were measured using an optical spectrum analyzer (AQ6375B, Yokogawa).

Table 2. Pump Coupling Efficiency, Propagation Losses and Pump Absorption in the Studied WGs

Guide width, μm	η_{coupl}, % (incl. δ_{loss}, meas.)	η_{coupl}, % (geom., calc.)	δ_{loss}, dB/cm (meas.)	η_{coupl}, % (excl. δ_{loss}, estim.)	δ_{loss}, dB/cm (Caird, estim.)	$\eta_{abs,L}$, %, T_{OC} = 50% (meas.)
	Pump (0.83 μm)	Pump	Pump (0.81 μm)	Pump (0.81 μm)	Laser (1.91 μm)	Pump (0.78 μm)
10	43.0±0.5	40.9	0.43±0.04	46.1±0.5	-	79.1±1
20	50.9±0.5	81.8	0.41±0.03	54.4±0.5	0.32±0.2	94.2±1
30	67.9±0.5	96.4	0.40±0.09	72.4±1	-	96.5±0.5
40	76.7±0.5	96.4	0.36±0.05	81.3±0.7	-	89.7±0.5
50	77.9±0.5	96.4	0.20±0.03	80.5±0.5	0.13±0.2	93.9±0.5

To determine the pump coupling efficiency, we coupled into the WGs the laser beam from the Ti:Sapphire laser tuned to 830 nm (out of the Tm^{3+} absorption) and monitored the power at the output facet. The pump coupling $\eta_{coupl} = P_{launch}/P_{inc}$ (P_{launch} is the launched pump power) was calculated excluding the propagation losses δ_{loss} estimated in Section 2.2. The η_{coupl} value includes Fresnel losses at the uncoated input facet of the crystal (T_{Fr} = 96.4%, as calculated using a refractive index of $LiYF_4$: n_e = 1.4722 at 830 nm). It is in the range of 80.5–46.1% for the 50-10 μm wide WGs and it is relatively close to the value obtained considering only the Fresnel losses and the geometrical overlap of the WG end-facet and the pump beam. As expected, η_{coupl} decreased for smaller widths of the guides.

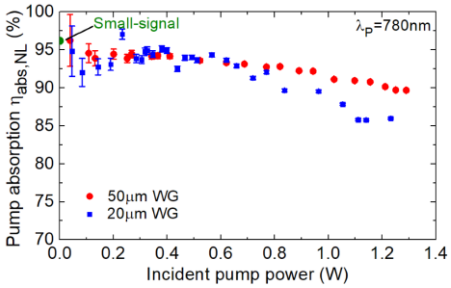

Fig. 8. Measured pump absorption under non-lasing conditions, $\eta_{abs,NL}$, in the 20 μm and 50 μm wide ridge WGs in 4 at.% Tm^{3+}:$LiYF_4$ as a function of the incident pump power. *Blue circle* – small-signal pump absorption.

For the 4.0 at.% Tm^{3+}:$LiYF_4$ crystal, the small-signal pump absorption $\eta_{abs,0}$ at 780 nm is close to unity. Indeed, $\eta_{abs,0} = 1 - \exp(-\sigma^{P}_{abs} N_{Tm} t) = 96.2\%$, where $\sigma^{P}_{abs} = 0.85\times10^{-20}$ cm^2 is the absorption cross-section at the pump wavelength λ_P for π-polarized light. The pump absorption under non-lasing conditions, $\eta_{abs,NL} = P_{abs}/P_{launch}$ (P_{abs} is the absorbed pump power) was determined from the pump-transmission (end-fire) measurements, see Fig. 8 for the example of the 20 μm and 50 μm wide WGs. The $\eta_{abs,NL}$ slowly decreased with the incident pump power due to the ground-state bleaching. At very small pump powers, $\eta_{abs,NL} \approx \eta_{abs,0}$. For estimating the absorbed pump power under lasing conditions P_{abs}, we have taken the $\eta_{abs,NL}$ value at the laser threshold (for each of the studied OCs). For example, for the 50 μm wide WG, the pump absorption slightly decreased from 94.5% for T_{OC} = 2% down to 93.9% for the highest studied T_{OC} = 50%. The pump saturation for the WG with a smaller width (20 μm) was stronger, as expressed by smaller values of $\eta_{abs,NL}$ for the same pump level, which is due to the higher light intensity in the guide. The values of pump absorption for the same T_{OC} = 50% and different WG width are compared in Table 2.

3.2 Laser performance

The laser operation was achieved for all the WGs when focusing the pump beam in the upper part of each of the guides. No laser emission was detected when the pump was focused in the bulk part of the sample. The experiments were performed in quasi-CW regime (duty cycle: 1:2) to diminish the thermal effects in thin passively-cooled ridges. The input-output dependences for the largest studied WG (width: 50 μm) are shown in Fig. 9(a). For T_{OC} = 50%, the laser generated a maximum output peak power of 381 mW at 1901-1929 nm (a broad emission spectrum) with a slope efficiency η of 42.2% with respect to the absorbed pump power P_{abs}. The laser threshold was at P_{abs} = 0.25 W and the optical-to-optical efficiency η_{opt} was 18.6% (as calculated vs. the pump power incident on the guide). For smaller output coupling, the laser threshold gradually decreased reaching P_{th} = 0.16 W for T_{OC} = 2%. For P_{abs} exceeding ~1 W, a thermal roll-over was observed in the input-output dependences. Thus, P_{abs} was limited to about 1.5 W to avoid thermal fracture of the guides.

The typical spectra of laser emission for the 50 μm wide WG and various transmissions of the output coupler are shown in Fig. 9(b). For all the OCs, the laser emission was linearly polarized (σ); the polarization was naturally selected by the gain anisotropy. The emission occurred at around ~1.91 μm for all the studied OCs in agreement with the gain spectra of Tm^{3+}:$LiYF_4$ for σ-polarization and small inversion ratios (see below).

For the sake of comparison, in Fig. 9(c,d), we show the input-output dependences and the typical spectra of laser emission for the smaller guide (width: 20 μm). The best performance for this WG corresponded to a maximum output peak power of 153 mW at 1884-1888 nm (in π polarization) with lower η = 25.3% and higher laser threshold P_{th} = 0.29 W (as compared to the 50 μm wide WG, for T_{OC} = 50%). The optical-to-optical efficiency was thus only 2.9%.

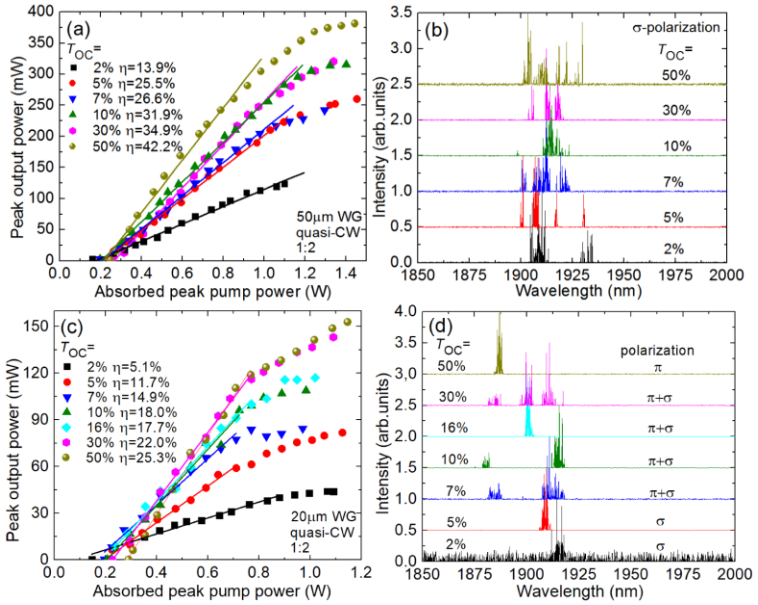

Fig. 9. Deep-diced Tm^{3+}:$LiYF_4$ ridge waveguide laser: (a,c) input-output dependences, η – slope efficiency; (b,d) typical laser emission spectra measured at (b) P_{abs} ~ 1.0 W and (d) P_{abs} ~ 0.6 W. Quasi-CW regime of operation with a duty cycle of 1:2. The channel width is (a,b) 50 μm and (c,d) 20 μm. The laser polarization is (a,b) σ and (c,d) σ or π.

The spectral behavior of the 20 μm wide WG laser was different from the 50 μm wide one, Fig. 9(d). For small output coupling, the laser operated in σ-polarization corresponding to the emission at ~1.91 μm (e.g., 1906-1911 nm for T_{OC} = 5%). For intermediate T_{OC} = 7 – 30%, two polarizations coexisted within the whole studied range of the absorbed pump power. As a result, the spectra contained emission lines within several regions (e.g., 1878-1882 & 1912-1918 nm for T_{OC} = 10%, with the short wavelength emission in π-polarization and the long-wavelength one in σ-polarization). Finally, for high T_{OC} = 50%, only π-polarized emission occurred.

Such polarization-switching is common for optically anisotropic (birefringent) laser crystals which exhibit similar gain cross-sections for two orthogonal principal light polarizations [30,31]. The switching between two polarizations can be promoted by change of the total intracavity losses (e.g., via the output coupling) or by polarization-dependent thermal lensing affecting the mode overlap efficiency or cavity stability. As a result, there may exist such levels of the cavity losses or pump powers for which two polarizations coexist leading to dual-wavelength (or multi-color) emission.

As pointed out above, the $^3F_4 \rightarrow {}^3H_6$ laser transition is a quasi-three-level scheme. The gain cross-sections, $\sigma_{gain} = \beta\sigma_{SE} - (1-\beta)\sigma_{abs}$, where $\beta = N_2(^3F_4)/N_{Tm}$ is the inversion ratio and N_2 is the population of the upper laser level ($^3F_4$), are thus calculated to conclude about the selected polarization and, consequently, the laser wavelength. Such a calculation for Tm^{3+}:$LiYF_4$ and π and σ polarizations is performed in Fig. 10. For small inversion ratios $\beta < 0.20$, the gain in σ-polarization is higher. A local peak in the gain spectra is found at ~1.91 μm and it is relatively broad (the gain bandwidth, determined as full width at half maximum, FWHM, $\Delta\lambda_g$ is ~60 nm for β = 0.20). For intermediate $0.20 < \beta < 0.30$, the peak gain cross-sections at ~1.91 (σ) and ~1.88 μm (π) are close. Finally, for high inversion ratios of $\beta > 0.35$, π-polarization corresponds to higher gain. The local peak at ~1.88 μm is narrower (as expressed by $\Delta\lambda_g$ ~35 nm).

These observations well explain the observed spectral behavior for narrow (20 μm) WG, considering that higher output coupling will lead to higher β. We believe that polarization-switching in such WGs can be controlled via a precise control of the propagation losses which

can be reached, e.g., by managing the cross-section profile of the guides or optimizing the dicing conditions.

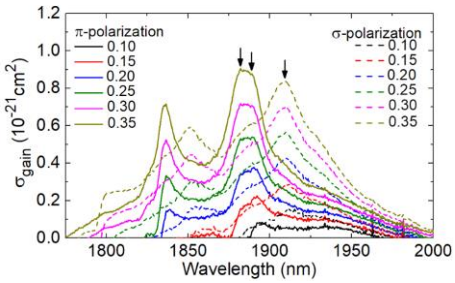

Fig. 10. Gain cross-sections, $\sigma_{gain} = \beta\sigma_{SE} - (1 - \beta)\sigma_{abs}$, for the $^3F_4 \leftrightarrow {}^3H_6$ transition of Tm^{3+} in $LiYF_4$ crystal for π and σ light polarizations. $\beta = N_2(^3F_4)/N_{Tm}$ is the inversion ratio, N_2 is the population of the upper laser level ($^3F_4$).

The waveguide propagation losses for the 20 μm and 50 μm wide WGs were estimated by means of the Caird analysis [32]: inverse of the slope efficiency, $1/\eta$, was plotted as a function of inverse of the output-coupling losses, $1/\gamma_{OC}$, where $\gamma_{OC} = -\ln(1 - T_{OC})$. The experimental points were fitted using the equation $(1/\eta) = (1/\eta_0)(1 + 2\gamma/\gamma_{OC})$ [33], where η_0 is the intrinsic slope efficiency and $\gamma = -\ln(1 - L)$, L is the single-pass passive loss. The best-fit values yields the propagation losses $\delta_{loss} = 4.34 \times L/t = 0.32 \pm 0.2$ dB/cm (20 μm WG) and 0.13 ± 0.2 dB/cm (50 μm WG).

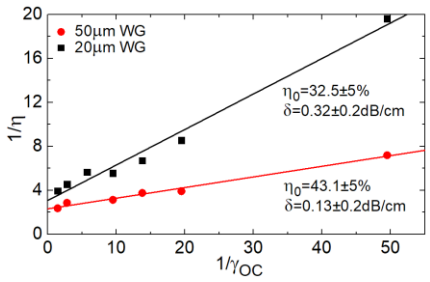

Fig. 11. Caird analysis: a plot of inverse of the slope efficiency, $1/\eta$, vs. inverse of the output-coupling losses, $1/\gamma_{OC}$, for 20 μm and 50 μm wide WGs: *symbols* – experimental data, *lines* - their fits for the determination of the propagation losses δ.

The determined values of δ_{loss} agree well with the estimations (cf. Table 2) from the pump-propagation measurements considering the difference in the light wavelength and modal profile (less transverse modes are expected for the laser emission because of much longer λ). We also confirm that the losses tend to increase for smaller guides.

In Fig. 12, we compare the laser performance for all the guides (10–50 μm) and the same output coupling (T_{OC} = 50%). The output power and the slope efficiency gradually decreased and the laser threshold increased for the smaller guides. For example, the 10 μm wide WG laser generated a peak power of 15 mW at 1878-1886 nm with η = 4.4% and a high laser threshold of 0.31 W. There exist several factors affecting the laser performance of smaller guides. First, the WG propagation losses increase as described above leading to both decreased η and higher P_{th}. Second, narrow guides exhibit severe thermal problems, so that the thermal roll-over in the output dependences occurs earlier. Finally, smaller guides provide higher intracavity laser intensities which, together with higher inversion needed to compensate for the higher passive losses, enhances the upconversion. Energy-transfer upconversion in Tm lasers is known to have a serious effect on the laser threshold [10]. Indirectly, it further enhances the heat dissipation.

The spectral behavior of the WGs lasers, Fig. 12(b), agrees with these considerations and the gain spectra. For small guides (10-20 μm) with higher passive losses, the laser operated in

π-polarization and for broader guides (30-50 μm) – in σ-polarization. The difference in the gain bandwidths also explains broader laser emission in the latter case.

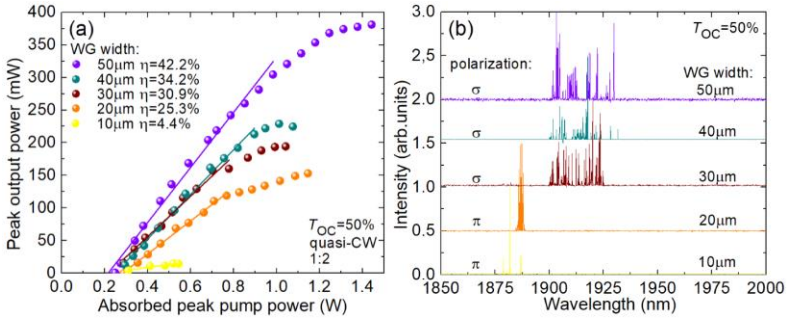

Fig. 12. Effect on the guide width on the laser performance of the deep-diced Tm^{3+}:$LiYF_4$ ridge waveguide laser: (a) input-output dependences, η – slope efficiency; (b) typical laser emission spectra measured at intermediate P_{abs}. Quasi-CW regime of operation with a duty cycle of 1:2. T_{OC} = 50%. The laser polarization is σ or π.

To verify our consideration about the thermal effects in the guides, we studied the laser performance of the 50 μm WG with the same output coupling (T_{OC} = 50%) but under different pump regimes, ranging from true CW to quasi-CW with various pump duty cycles (between 1:2 to 1:12), Fig. 13. The CW laser generated only 34 mW and the lasing was ceased for P_{abs} > 0.5 W. For the quasi-CW operation regimes with decreasing the duty cycle down to 1:12 (thus reducing the heat loading), the input-output dependence gradually approached the linear one, so that the power scaling was limited only by the available pump. For the 1:12 duty cycle, the maximum peak output power reached 684 mW with η = 53.3%. Note that the laser threshold was almost independent on the pump modulation.

The determined value of the slope efficiency exceeds the Stokes limit under lasing conditions, $\eta_{St,L} = \lambda_P/\lambda_L$ = 40.8% (λ_L ~1910 nm is the laser wavelength) indicating the action of cross-relaxation for adjacent Tm^{3+} ions increasing the pump quantum efficiency [26].

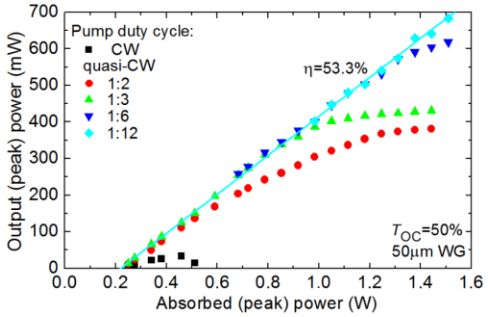

Fig. 13. Evidence of thermal effects in deep-diced Tm^{3+}:$LiYF_4$ ridge waveguide laser: input-output dependences measured for true CW and quasi-CW operation regimes. WG with a width of 50 μm, T_{OC} = 50%. η – slope efficiency for the duty cycle of 1:12.

4. Conclusions

To conclude, we report on a novel approach to fabricate ridge WGs with a large surface area (high depth-to-width aspect ratio, well above 1) in bulk fluoride crystals based on precision diamond saw dicing. This method has the following advantages: (i) it is relatively simple from a technological point of view, (ii) it provides an appropriate precision, an easy control of the geometrical profile and a fast writing speed, (iii) it ensures strong guiding both in the passive and laser-active regimes of light propagation without leakage of the modes in the bulk volume, (iv) it provides low roughness of the guide walls and, consequently, relatively low passive

losses, potentially down to 0.1 dB/cm, and (v) it can be applied for a wide variety of materials with different RE^{3+} dopants. A single-transverse-mode laser operation is expected with a proper design of the geometrical profile of the channels; it will be also facilitated by the gain guiding in the case of quasi-three-level lasers. Further studies are however needed to clarify the nature and the absolute value of the expected refractive index variation in the guides with respect to the bulk volume.

In the particular case of deep-diced Tm^{3+}:$LiYF_4$ WGs, the main limitation for power scaling is the thermal issues. It can be overcame by better thermal management, e.g., by applying active cooling. Other strategies may involve using higher Tm^{3+} doping levels for more efficient cross-relaxation reaching a pump quantum efficiency of 2 (for the conventional pumping at ~780 nm) or employing in-band pumping directly to the $^3F_4$ upper laser level. Bulk Tm^{3+}:$LiYF_4$ crystals of laser quality with high doping levels (7 – 15 at.% Tm) are easily accessible. An optimization of the writing depth may also greatly improve the thermal behavior of the guides.

Funding

French Agence Nationale de la Recherche (ANR) (CEPAGE ANR-AAP-CE2; LabEx EMC3 (ANR-10-LABX-09-01); SPLENDID2 (ANR-19-CE08-0028)); Normandie region; European Community funds FEDER ("NOVAMAT").

Acknowledgments

This work was partly supported by the French RENATECH network and its FEMTO-ST technological facility.

Disclosures

The authors declare no conflicts of interest.

References

1. P. Loiko, R. Thouroude, R. Soulard, L. Guillemot, G. Brasse, B. Guichardaz, A. Braud, A. Hideur, M. Laroche, H. Gilles, and P. Camy, "In-band pumping of Tm:$LiYF_4$ channel waveguide: a power scaling strategy for ~2 μm waveguide lasers," Opt. Lett. **44**(12), 3010-3013 (2019).
2. W. Bolaños, F. Starecki, A. Braud, J.-L. Doualan, R. Moncorgé, and P. Camy, "2.8 W end-pumped Yb^{3+}:$LiYF_4$ waveguide laser," Opt. Lett. **38**(24), 5377-5380 (2013).
3. Y. Ren, C. Cheng, Y. Jia, Y. Jiao, D. Li, M. D. Mackenzie, A. K. Kar, and F. Chen, "Switchable single-dual-wavelength Yb,Na:CaF_2 waveguide lasers operating in continuous-wave and pulsed regimes," Opt. Mater. Express ^{8}(6), 1633-1641 (2018).
4. P. Loiko, R. Soulard, G. Brasse, J. L. Doulan, A. Braud, A. Tyazhev, A. Hideur, and P. Camy, "Tm,Ho:$LiYF_4$ planar waveguide laser at 2.05 μm," Opt. Lett. **43**(18), 4341-4344 (2018).
5. P. Loiko, R. Soulard, E. Kifle, L. Guillemot, G. Brasse, A. Benayad, J.-L. Doualan, A. Braud, M. Aguiló, F. Díaz, X. Mateos, and P. Camy, "Ytterbium calcium fluoride waveguide laser," Opt. Express **27**(9), 12647-12658 (2019).
6. R. L. Aggarwal, D. J. Ripin, J. R. Ochoa, and T. Y. Fan, "Measurement of thermo-optic properties of $Y_3Al_5O_{12}$, $Lu_3Al_5O_{12}$, $YAlO_3$, $LiYF_4$, $LiLuF_4$, BaY_2F_8, $KGd(WO_4)_2$, and $KY(WO_4)_2$ laser crystals in the 80–300 K temperature range," J. Appl. Phys. **98**(10), 103514-1-14 (2005).
7. N. P. Barnes and D. J. Gettemy, "Temperature variation of the refractive indices of yttrium lithium fluoride," J. Opt. Soc. Am. **70**(10), 1244-1247 (1980).
8. S. A. Miller, H. E. Rast, and H. H. Caspers, "Lattice vibrations of $LiYF_4$," J. Chem. Phys. **52**(8), 4172-4175 (1970).
9. B. M. Walsh, N. P. Barnes, and B. Di Bartolo, "Branching ratios, cross sections, and radiative lifetimes of rare earth ions in solids: Application to Tm^{3+} and Ho^{3+} ions in $LiYF_4$," J. Appl. Phys. **3**(5), 2772–2787 (1998).
10. S. So, J. I. Mackenzie, D. P. Sheperd, W. A. Clarkson, J. G. Betterton, and E. K. Gorton, "A power-scaling strategy for longitudinally diode-pumped Tm:YLF lasers," Appl. Phys. B **84**(3), 389–393 (2006).
11. P. Loiko, J. M. Serres, X. Mateos, S. Tacchini, M. Tonelli, S. Veronesi, D. Parisi, A. Di Lieto, K. Yumashev, U. Griebner, and V. Petrov, "Comparative spectroscopic and thermo-optic study of Tm:$LiLnF_4$ (Ln = Y, Gd, and Lu) crystals for highly-efficient microchip lasers at ~2 μm," Opt. Mater. Express **7**(3), 844-854 (2017).
12. P. Loiko, R. Soulard, L. Guillemot, G. Brasse, J. L. Doualan, A. Braud, A. Tyazhev, A. Hideur, F. Druon, and P. Camy, "Efficient Tm:$LiYF_4$ lasers at ~2.3 μm: Effect of energy-transfer upconversion," IEEE J. Quantum Electron. **55**(6), 1700212-1-12 (2019).

13. R. Soulard, M. Salhi, G. Brasse, P. Loiko, J. L. Doualan, L. Guillemot, A. Braud, A. Tyazhev, A. Hideur, and P. Camy, “Laser operation of highly-doped Tm:$LiYF_4$ epitaxies: towards thin-disk lasers,” Opt. Express **27**(6), 9287-9301 (2019).
14. B. Cockayne, J. G. Plant, and R. A. Clay, “The Czochralski growth and laser characteristics of Li(Y,Er,Tm,Ho)F_4 and Li(Lu,Er,Tm,Ho)F_4 scheelite single crystals,” J. Cryst. Growth **54**(3), 407-413 (1981).
15. F. Starecki, W. Bolaños, G. Brasse, A. Benayad, M. Morales, J. L. Doualan, A. Braud, R. Moncorgé, and P. Camy, “Rare earth doped $LiYF_4$ single crystalline films grown by liquid phase epitaxy for the fabrication of planar waveguide lasers,” J. Cryst. Growth **401**, 537-541 (2014).
16. W. Bolanos, F. Starecki, A. Benayad, G. Brasse, V. Ménard, J.-L. Doualan, A. Braud, R. Moncorgé, and P. Camy, "Tm:$LiYF_4$ planar waveguide laser at 1.9 μm," Opt. Lett. **37**(19), 4032-4034 (2012).
17. D. Geskus, S. Aravazhi, C. Grivas, K. Wörhoff, and M. Pollnau, “Microstructured $KY(WO_4)_2$:Gd^{3+},Lu^{3+},Yb^{3+} channel waveguide laser,” Opt. Express 18(9), 8853-8858 (2010).
18. P. Loiko, R. Soulard, G. Brasse, J. L. Doualan, B. Guichardaz, A. Braud, A. Tyazhev, A., Hideur, and P. Camy, “Watt-level Tm:$LiYF_4$ channel waveguide laser produced by diamond saw dicing,” Opt. Express **26**(19), 24653-24662 (2018).
19. G. F. Chen, X. Zhao, Y. Sun, C. He, M. C. Tan, and D. T. Tan, “Low loss nanostructured polymers for chip-scale waveguide amplifiers,” Sci. Rep. **7**, 3366-1-8 (2017).
20. S. H. Waeselmann, C. E. Rüter, D. Kip, C. Kränkel, and G. Huber, “Nd:sapphire channel waveguide laser,” Opt. Mater. Express 7(7), 2361-2367 (2017).
21. Y. Jia, C. E. Rüter, S. Akhmadaliev, S. Zhou, F. Chen, and D. Kip, "Ridge waveguide lasers in Nd:YAG crystals produced by combining swift heavy ion irradiation and precise diamond blade dicing," Opt. Mater. Express **3**(4), 433-438 (2013).
22. E. Kifle, P. Loiko, U. Griebner, V. Petrov, P. Camy, A. Braud, M. Aguiló, F. Díaz, and X. Mateos, “Diamond saw dicing of thulium channel waveguide lasers in monoclinic crystalline films,” Opt. Lett. **44**(7), 1596-1599 (2019).
23. C. Chen, C. E. Rüter, M. F. Volk, C. Chen, Z. Shang, Q. Lu, S. Akhmadaliev, S. Zhou, F. Chen, and D. Kip, "Second harmonic generation of diamond-blade diced $KTiOPO_4$ ridge waveguides," Opt. Express **24**(15), 16434-16439 (2016).
24. J. Sun, and C. Xu, “466 mW green light generation using annealed proton-exchanged periodically poled MgO:$LiNbO_3$ ridge waveguides,” Opt. Lett. **37**(11), 2028-2030 (2012).
25. N. Courjal, B. Guichardaz, G. Ulliac, J. Y. Rauch, B. Sadani, H. H. Lu, and M. P. Bernal, “High aspect ratio lithium niobate ridge waveguides fabricated by optical grade dicing,” J. Phys. D: Appl. Phys. **44**(30), 305101 (2011).
26. K. van Dalfsen, S. Aravazhi, C. Grivas, S. M. García-Blanco, and M. Pollnau, "Thulium channel waveguide laser with 1.6 W of output power and ~80% slope efficiency," Opt. Lett. **39**(15), 4380-4383 (2014).
27. J. I. Mackenzie, S. C. Mitchell, R. J. Beach, H. E. Meissner, and D. P. Shepherd, “15 W diode-side-pumped Tm:YAG waveguide laser at 2 μm,” Electron. Lett. **37**(14), 898-899 (2001).
28. D. P. Shepherd, S. J. Hettrick, C. Li, J. I. Mackenzie, R. J. Beach, S. C. Mitchell, and H. E. Meissner, “High-power planar dielectric waveguide lasers,” J. Phys. D: Appl. Phys. **34**(16), 2420 (2001).
29. O. V. Ivanova, R. Stoffer, and M. Hammer, “A variational mode solver for optical waveguides based on quasianalytical vectorial slab mode expansion,” University of Twente, technical report (2009, pp. 1–19).
30. F. Druon, M. Olivier, A. Jaffrès, P. Loiseau, N. Aubry, J. DidierJean, F. Balembois, B. Viana, and P. Georges, "Magic mode switching in Yb:$CaGdAlO_4$ laser under high pump power," Opt. Lett. **38**(20), 4138-4141 (2013).
31. P.A. Loiko, X. Mateos, N.V. Kuleshov, A.A. Pavlyuk, K.V. Yumashev, V. Petrov, U. Griebner, M. Aguiló, and F. Díaz, “Thermal-lens-driven effects in N_g-cut Yb- and Tm-doped monoclinic $KLu(WO_4)_2$ crystals,” IEEE J. Quantum Electron. **50**(8), 669-676 (2014).
32. J. A. Caird, S. A. Payne, P. R. Staber, A. J. Ramponi, L. L. Chase, and W. F. Krupke, “Quantum electronic properties of the $Na_3Ga_2Li_3F_{12}$:Cr^{3+} laser,” IEEE J. Quantum Electron. **24**(6), 1077–1099 (1988).
33. J. Morris, N. K. Stevenson, H. T. Bookey, A. K. Kar, C. T. A. Brown, J.-M. Hopkins, M. D. Dawson, and A. A. Lagatsky, “1.9 μm waveguide laser fabricated by ultrafast laser inscription in Tm:Lu_2O_3 ceramic,” Opt. Express **25**(13), 14910–14917 (2017).